Extreme Mechanics Letters 30 (2019) 100496

Contents lists available at ScienceDirect

Extreme Mechanics Letters

journal homepage: www.elsevier.com/locate/eml

Suction effects of crater arrays

Liu Wang [a], Kyoung-Ho Ha [b], Shutao Qiao [a], Nanshu Lu [a,b,c,d,*]

[a] Center for Mechanics of Solids, Structures and Materials, Department of Aerospace Engineering and Engineering Mechanics, The University of Texas at Austin, Austin, TX 78712, United States
[b] Department of Mechanical Engineering, The University of Texas at Austin, Austin, TX 78712, United States
[c] Department of Biomedical Engineering, The University of Texas at Austin, Austin, TX 78712, United States
[d] Texas Materials Institute, The University of Texas at Austin, Austin, TX 78712, United States

ARTICLE INFO

Article history:
Received 13 May 2019
Received in revised form 7 June 2019
Accepted 8 June 2019
Available online 12 June 2019

Keywords:
Dry adhesive
Suction
Crater array
Area fraction
Pattern

ABSTRACT

There are emerging experimental evidence that craters engineered on polymer surfaces can enhance attachment via suction effects. In the past, we have developed a theoretical framework for quantifying suction forces produced by an isolated crater, i.e., a crater resides on the surface of a semi-infinite solid, under both dry and wet conditions. Following this framework, in this paper, we investigate the suction effects produced by an array of craters. As arrays of both cylinder-shaped (CS) and spherical-cap-shaped (SCS) craters have been reported in the literature, we first make a comparison between them and find that the SCS craters outperform the CS craters. Thereafter, we focus on SCS crater arrays and study the effects of area fraction as well as different types of array patterns (square vs. hexagon). Assuming a given polymer matrix, using finite element modeling (FEM), we find that for both patterns, when the preload is small, suction force increases with crater area fraction. However, when the preload is large (e.g., when the craters attain full closure), non-monotonic relationship between suction force and crater area fraction exists. This is because suction force is governed by not only the pressure drop but also the projected area of the crater after unloading.

1. Introduction

Conventional pressure-sensitive adhesives (PSAs) employ a thin layer of viscoelastic bonding agent (e.g., acrylics, polyesters, etc.) that can instantaneously form strong bond to the adherend when pressure is applied [1–4]. However, such PSAs face limitations such as susceptibility to impurities and limited reusability. PSA-based bio-adhesives may also cause skin irritation [5], contact dermatitis [6] and damage [7] due to the bonding agent.

To develop chemical-free adhesives, a.k.a. dry adhesives or physical adhesives, with strong bonding and high reusability, a wealth of attention has been paid to engineering micro-structures on polymer surfaces in the last two decades [8–13]. So far, gecko-inspired micro-pillar system is the most prevailing dry adhesives [14–18]. In reminiscence of the hierarchical micro-fibril structure on gecko toe pads, man-made micro-pillar arrays have demonstrated enhanced adhesion over their flat counterparts because of multiple mechanisms [8,19–23]. However, the fabrication of either hierarchical [24] or composite [25] micro-pillars involves quite complicated processes and the adhesive strength is usually fixed once fabricated [26–28]. Also, micro-pillars are prone to collapse and fracture due to their slenderness [8,21,29–31], which compromises their reusability and scratch resistance. In addition, it has been reported that wet surfaces or aquatic environment impairs the performance of micro-pillar-enabled adhesives [32–34].

As a result, arrays of micro-craters (i.e. dimples engineered on polymer surfaces) recently emerged as an alternative surface texture for reversible adhesion. Emerging experimental results indicate that micro-craters on polymer surface can enhance adhesion. For instance, Akerboom et al. fabricated close-packed nano-dimples on polydimethylsiloxane (PDMS) (Fig. 1a) and found that the normal pull-off force is improved compared with its flat PDMS counterpart [35]. Choi et al. have observed similar improvement in the shear pull-off tests on a multilayer PDMS specimen whose surface was engineered with an array of 1-μm-diameter craters [36]. Chang et al. created an array of submicron-diameter craters on UV resin and measured its adhesive shear strength on silicon wafer to be as high as 750 kPa [37]. Emulating the design principle of octopus suckers [38], micro-scale crater arrays with interior dome-like protuberance have been created by Baik et al. to achieve strong adhesion in both dry and aquatic environment [39]. Baik et al. also engineered micro-pillars with concave tip geometry, demonstrating enhanced dry/wet adhesion performances against both smooth and rough surfaces [40]. Most recently, Tinnemann et al. explicitly claimed that the suction

* Correspondence to: 210 E. 24th St, Austin, TX 78712, United States.
E-mail address: nanshulu@utexas.edu (N. Lu).

https://doi.org/10.1016/j.eml.2019.100496
2352-4316/

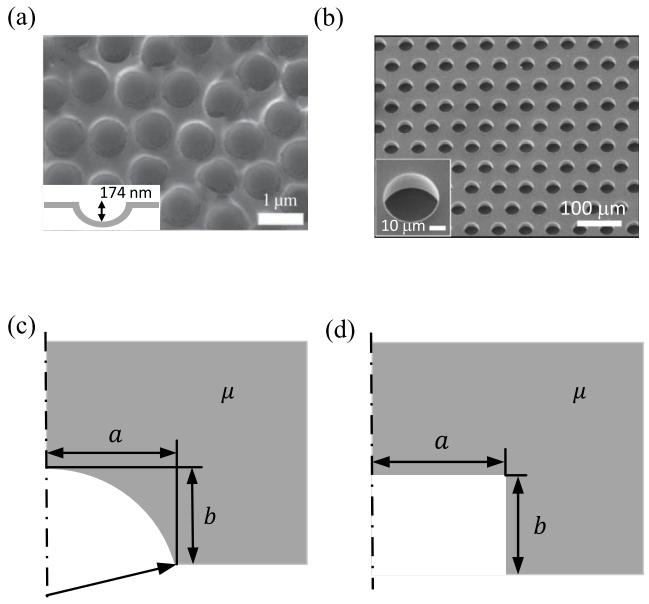

Fig. 1. Scanning electron microscope (SEM) images of micro-crater arrays with (a) dome-like crater where the inset illustrates the cross-sectional profile (reproduced from Ref. [35] with permission of The Royal Society interface) and (b) cylinder-shaped crater where the inset gives a blown-up view (reproduced from Ref. [39] with permission of Nature). Axisymmetric schematics for (c) spherical-cap-shaped (SCS) crater and (d) cylinder-shaped (CS) crater. The crater radius and height are denoted as a and b, respectively. The polymer matrix is assumed to be incompressible neo-Hookean material with shear modulus μ.

effect contributes to 20% of the total adhesive forces of micro-pillar arrays with mushroom tip according to their experimental measurements [41].

Advantages of crater-enabled dry adhesives include pressure-sensitive tunable adhesive strength, strong adhesion underwater or with wet surfaces, quick and easy release, reusability, as well as biocompatibility as they do not require any chemical-based bonding agent. As a result, they can be applied on robotics for wall climbing [11,42], object manipulation [37] or wafer handling [43], biomedical devices for secure but releasable attachment with bio-tissue [7,44], or even on cell phone cases for temporary mounting [45].

Despite rapid growth in experimental demonstration of cratered surfaces, fundamental and quantitative mechanistic understanding of such systems is still limited. It is now widely accepted that cratered surfaces promote adhesive strength primarily through pressure drop inside the craters, i.e., suction. Shapes of crater can play an essential role in suction generation. The most common crater shape is concave domes, including both shallow [35] and deep [36,37,46] craters (Fig. 1a). Experimentally, Nanni et al. found that under the same compressive load, surfaces engineered with shallow domes yield higher pull-off forces than the ones with deeper domes [47]. Apart from concave domes, craters can also be manufactured into cuboid or cylindrical shapes. Nanni et al. also measured the adhesion of cuboid-shaped crater arrays with different crater depths. Again, they observed higher pull-off forces for shallower craters when subjected to the same compressive load [47]. Cylinder-shaped (CS) crater arrays (Fig. 1b) were investigated by Baik et al. who demonstrated that CS crater arrays exhibit normal adhesive strength comparable to those engineered with an interior protuberance inspired by octopus [39]. This finding implies that CS crater arrays are also capable of producing high adhesion under dry condition. Herein, a quantitative comparison of the suction forces generated by dome-like craters vs. CS craters is of great interest. Schematics of a representative dome-like crater – a spherical-cap-shaped (SCS) crater and a CS crater are displayed in Fig. 1c and Fig. 1d in which the crater base radius and height are labeled as a and b, respectively.

Aside from crater shape, crater area fraction, ϕ, defined as the ratio of the projected crater area to the overall area of the surface, is another crucial geometric parameter that governs the adhesion performance. For instance, Nanni et al. measured the adhesion of elastomeric surfaces structured with micro-dimples of different area fractions [47]. They observed that the adhesive strength exhibits a non-monotonic dependence on the crater area fraction, which remains a conundrum till now. It is also worth noting that crater arrays can be in square pattern [47] or hexagon pattern [35,39]. So far, no available study discusses how different array patterns would affect the suction effects of crater arrays. Therefore, the goal of this paper is to use experimentally validated finite element modeling (FEM) approach to quantitatively investigate the effects of crater shape, area fraction of crater array, as well as array pattern on suction generation.

In the past, we have developed a framework for quantifying the suction effects in cratered surfaces [48]. The suction effects of SCS craters with various aspect ratios b/a under both dry [48] and wet conditions [49] have been quantitatively investigated. We have also revealed how surface tension would affect the suction force generated by miniaturized craters [50]. In these studies, craters were assumed to be isolated. The results obtained for isolated craters can also be applied to a crater array if the size of an individual crater in a crater array is much smaller than the crater spacing and specimen dimensions, so that the interaction between craters is minimal. Following the same framework, in this paper, we will focus on crater arrays where there will be interplay between crater size and crater spacing, i.e. when area fraction matters. We will investigate three primary geometric features of a cratered surface — crater shape, crater area fraction, and crater array pattern. Moreover, suction forces as a function of the preload will be systematically analyzed.

This paper is organized as follows. Section 2 provides a brief recap of the theoretical framework we previously established for analyzing suction forces generated by craters. Section 3 studies the shape effect of an isolated crater, followed by analysis on crater array in Section 4. Concluding remarks are offered in Section 5.

2. Theoretical framework

Previously we have developed a theoretical framework to analyze suction generated by craters [48,49] so we will briefly describe it here. We suppose that the specimen is made of rubber which is capable of sustaining large elastic deformation and neglect surface tension effect [50–52]. The loading–unloading process is illustrated using a quarter of the crater in Figs. 2a–2c. Initially, the air inside the crater is in equilibrium with the air in the ambient, and it is characterized by the pressure p_0, volume V_0 and number of molecules N_0 (Fig. 2a). The suction effect is realized in the following two steps:

1. Step I: the specimen is subjected to an average compressive stress, $\overline{\sigma}_{pre}$, named the preload, against a rigid flat plate (not shown in Fig. 2b), such that air is squeezed out of the crater. At the end of this step, the remaining air in the carter is characterized by the triplet (p_1, V_1, N_1) (Stage 1, Fig. 2b).
2. Step II: the specimen is unloaded and the crater springs back. This action results in a pressure drop inside the crater which produces the suction force. At the end of this step, the air in the crater is characterized by the triplet

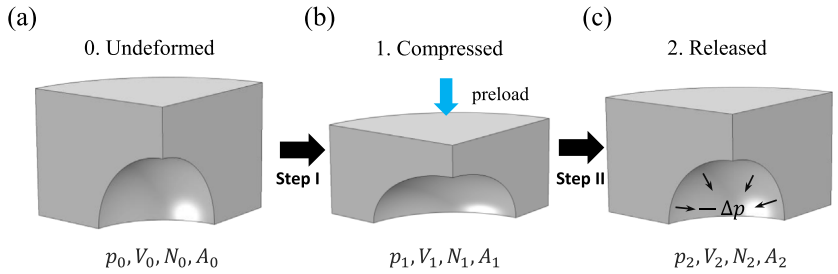

Fig. 2. Schematics illustrating the loading–unloading process of an isolated crater. (a) Stage 0: the crater initially has a volume V_0 and projected area A_0. (b) Stage 1: preload is applied on the specimen to squeeze air out of the crater such that crater volume reduces to V_1 with projected area A_1; (c) Stage 2: crater volume recovers to V_2 with projected are A_2 after unloading. p and N denote the pressure and number of air molecules inside the crater at each stage.

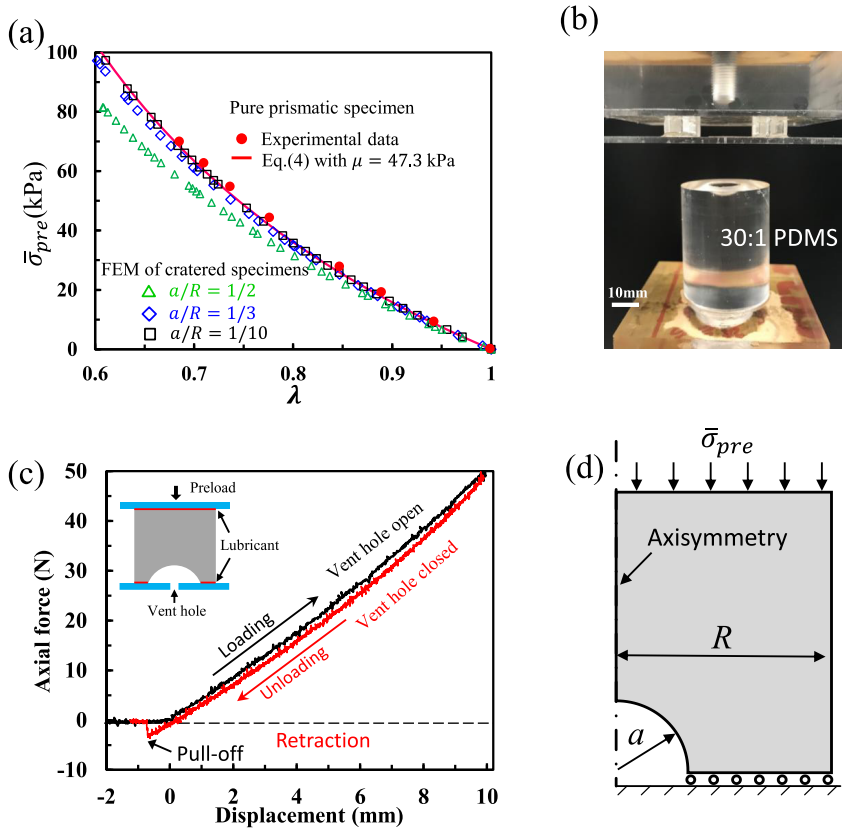

Fig. 3. (a) Preload–stretch relationship for pure prismatic specimen and cratered specimens. Red dots are experimental data for pure prismatic specimen whose behavior can be successfully captured by the red curve, which represents an incompressible neo-Hookean material model given by Eq. (4) with shear modulus $\mu = 47.3$ kPa. Hollow markers are FEM results for cratered specimens with different a/R ratios. (b) Experimental set-up of a cylindrical specimen with a SCS crater of aspect ratio 2/3. (c) A representative experimental load–displacement curve for the entire loading–unloading-retraction process. The horizontal dashed line marks full unloading, i.e., Stage 2. (d) A schematic of the axisymmetric FEM model for isolated craters with lubricated interfaces.

(p_2, V_2, N_2) (Stage 2, Fig. 2c). Accordingly, the pressure drop is

$$-\Delta p = p_1 - p_2$$

and the suction force is

$$F = -\Delta p A_2 \tag{1}$$

where A_2 is the projected area of the crater at Stage 2.

Key assumptions adopted in this framework are:

(a) The air flows freely out of the crater upon loading (Step 1), so that $p_1 = p_0$.
(b) No air exchange takes place upon unloading (Step 2), so that $N_2 = N_1$.
(c) The entire process is isothermal and the air is an ideal gas, so that $p_1 V_1 = p_2 V_2$.

As a result, the pressure drop can be related to the crater volumes as

$$-\Delta p = \left(1 - \frac{V_1}{V_2}\right) p_0 \tag{2}$$

Therefore, the suction force becomes

$$F = \left(1 - \frac{V_1}{V_2}\right) p_0 A_2 \tag{3}$$

The first assumption that the air can flow out freely when compressed is inspired by prior works on thin-walled suction cups [53–55]. In these models [53–55], analytical relationship between preload and suction-cup deformation has been obtained by neglecting gas resistance during compression. As for the second assumption that there is no leakage during unloading, it is consistent with experimental observations for thin-walled suction

cups [53–55] as well as surface craters [39]. The third assumption of ideal gas is widely adopted for air at room temperature. It is worth pointing out that craters are rather different from thin-walled suction cups as craters are arrays of dimples on the surface which are surrounded by thick walls formed by the polymer matrix as illustrated by Fig. 2.

3. Effects of crater shape

In this section, we study the effects of crater shape using isolated craters. The following representative shapes will be examined and compared: SCS craters with aspect ratio $b/a = 2/3$ and 1 and CS craters with aspect ratio $b/a = 2/3$ and 1. The aspect ratio $b/a = 2/3$ is intentionally selected since the initial volume of a CS crater with $b/a = 2/3$ is identical to that of a SCS crater with aspect ratio $b/a = 1$. Both FEM and experiments were carried out to quantitatively characterize the suction effects of SCS craters for the purpose of validation. Afterwards, only FEM would be performed for isolated CS craters as well as SCS crater arrays.

3.1. Experiments

Polydimethylsiloxane (PDMS, Sylgard 184 Dow Corning) with the base-to-curing-agent mass ratio equal to 30:1 was cured at 70° for 12 h to mold three specimens. The first sample was a pure cylindrical prism whose radius and height were $R = 12.7$mm and $H = 50.8$ mm. The other two specimens were cylindrical prisms with the same dimensions but endowed with a SCS crater of radius $a/R = 1/3$ at the center of the circular face. The first SCS crater was a hemi-sphere (i.e., $b/a = 1$) and the second SCS crater had an aspect ratio of $b/a = 2/3$. The design $a/R = 1/3$ corresponds to $\phi = 11.1\%$, which would suffice for the assumption of isolated craters (see Section 0 for details). We first carried out a uniaxial compression test on the pure cylindrical prism for the measurement of material properties using a Mechanical Testing System (MTS Servohydraulic load frame with Instron 8500R controller and Omega LCHD-50 load cell). The top and bottom surfaces of the specimen were lubricated by performance oil (Fellowes Powershred Performance Shredder Oil) such that the specimen could be subjected to uniaxial stress. The measured axial load–displacement data was converted to the nominal stress σ versus the principal stretch λ data and fitted by the incompressible neo-Hookean model

$$\sigma = \mu\left(\lambda - \frac{1}{\lambda^2}\right) \tag{4}$$

where shear modulus μ is the fitting parameter. Measured and fitted σ vs. λ results are plotted as red markers and a red curve in Fig. 3a, respectively. A fitting function with $\mu = 47.3$ kPa agrees well with experimental data.

Since direct measurement of the suction force at full unloading, i.e., Eq. (3), is difficult, we performed the loading–unloading-retraction experiments and measured the pull-off force $F_{pull-off}$ instead. To realize experimental conditions that well represent the adopted assumptions, we built a special platform as shown by an experimental picture in Fig. 3b. The cratered specimen was compressed against a stiff acrylic platform where a tiny ventilation hole has been drilled for releasing and trapping air inside the crater, as illustrated by the schematic inset in Fig. 3b. During the loading step, the hole was opened such that air was able to flow out freely, which is consistent with Assumption (a). During the unloading step, consistent with Assumption (b), the hole was sealed so that air was trapped in the crater. Both top and bottom surfaces were well-lubricated as before. Without the vent hole, we noticed that there was resistance against air flowing out. Therefore, our assumptions and experimental setup are idealized.

A representative experimental loading–unloading-retraction curve is given in Fig. 3c. The loading, unloading, and retraction stages, as well as the pull-off point are labeled in Fig. 3c. As has been proposed in our previous papers [48,49], one simple way to determine the suction force F' at pull-off is by calculating the difference

$$F' = F_{pull-off} - \sigma_{th}A(1-\phi) \tag{5}$$

where $A = \pi R^2$ is the area of the circular face of the specimen, and σ_{th} is the adhesive strength of lubricated PDMS/platform interface. According to our previous experimental measurements [48,49], $\sigma_{th} \approx 1.1$ kPa and is independent of preload. Note that the definition of the suction force in FEM, i.e., F given by Eq. (3) at full unloading, is slightly different from that in experiment, i.e., F' given by Eq. (5) at pull-off point. Experimentally measured pull-off force F involves a retraction strain beyond the full unloading. When retraction strain is small enough under small preload, $F' \approx F$. However, the retraction strain increases with preload, causing F' to deviate from F under large preload. Experimental and simulation results, as well as in-depth discussion, will be offered in Section 3.3.

3.2. Simulation

Following experimental data for the pure prismatic specimens, we assume that the cratered specimens are also taking the incompressible neo-Hookean constitutive law with shear modulus $\mu = 47.3$ kPa. A schematic of the FEM is depicted in Fig. 3d where a hemispherical crater (i.e., $b/a = 1$) was adopted. Three axisymmetric models with $a/R = 1/2, 1/3, 1/10$ were first built to examine the criterion for isolated craters. The lubricated specimen/substrate interface was assumed to be frictionless, i.e., roller boundary condition in simulation. The σ vs. λ results under uniaxial compression were extracted from FEM and plotted in Fig. 3a as open markers, along with measured and fitted results for the pure prismatic specimen. Note that the pure prismatic specimen represents the extreme case of $\phi = 0$, which can be regarded as isolated craters whose $a/R \to 0$. When $a/R = 1/10$, corresponding to $\phi = 1\%$, the FEM results shown by the black square makers overlap with that of $\phi = 0$. Actually, when $a/R = 1/3$ (i.e., $\phi = 11.1\%$), FEM results (blue diamond markers) also agree reasonably well with that from the pure prismatic specimen, suggesting that even $a/R = 1/3$ can be approximately treated as isolated craters. Hence from now on, we consider carters with $\phi \leq 11.1\%$ to be isolated craters. By fixing $a/R = 1/3$, FEM were carried out for the following four crater geometries: two SCS craters with $b/a = 2/3$ and 1; and other two CS craters with $b/a = 2/3$ and 1. All FEM were conducted using commercial FEM package ABAQUS 6.13 in which the built-in function *FLUID CAVITY was implemented to model the ideal gas behavior inside the craters.

3.3. Results

The normalized suction force produced by an isolated crater $F_{\text{iso}}/(p_0A_0)$ as a function of preload, $\overline{\sigma}_{pre}$, are given in Fig. 4. Solid and dashed curves represent the FEM results for SCS and CS craters, respectively. Dots with error bars are experimental data of SCS craters. Craters with $b/a = 2/3$ are represented by blue and those with $b/a = 1$ are in red, respectively. We conducted a series of loading–unloading-retraction tests on SCS craters with aspect ratios of $b/a = 2/3$ and 1 using MTS. The pull-off forces were measured and the suction forces were calculated according to Eq. (5). It is evident that FEM results are in good agreement

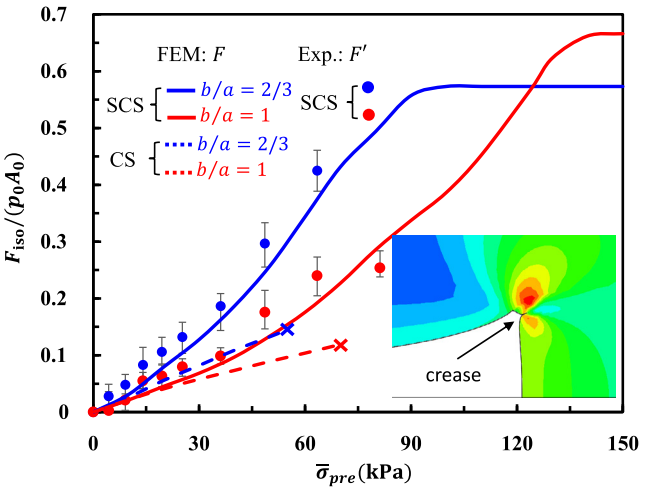

Fig. 4. Normalized suction forces of isolated craters as a function of preload. FEM results of SCS and CS isolated craters are presented by solid and dashed curves, respectively. Experimental results for SCS are shown by solid dots. Blue represents craters with aspect ratio of 2/3 and red for aspect ratio of 1. The inset exhibits the crease instability of CS crater with $b/a = 1$ at $\overline{\sigma}_{pre} = 70$ kPa . (For interpretation of the references to color in this figure legend, the reader is referred to the web version of this article.)

with experimental data, suggesting that $F' \approx F$ when the preload is small. Such an agreement also justifies the applicability of the simulations for characterizing more general situations, such as crater arrays. Note that experimental data is only presented up to 80 kPa. This is because large discrepancy between experimental data F' are numerical results F has been found when $\overline{\sigma}_{pre} > 80$ kPa. As mentioned before, such discrepancy originates from the different definitions of suction forces, i.e., F in Eq. (3) versus F' in Eq. (5), rather than the simulation itself. The retraction strain beyond full unloading applies an extra tensile strain on the specimen thus changes the suction force. In our recent work [49], we have shown that modified FEM results by adding experimentally measured retraction strain after full unloading indeed agrees well with measured suction force at pull-off point. Therefore, we believe that the entire FEM curves in Fig. 4 are able to capture the true suction forces at the end of unloading.

Several important observations can be made from the FEM curves in Fig. 4. First, for all cases, suction force increases as preload grows before craters reach full closure because large preload yields small crater volume at the end of loading, i.e., small V_1 leads to large F according to Eq. (3). Note that it is easier for SCS craters to attain full closure and achieve the maximum suction force, as shown by the plateau of the solid curves. By contrast, localized crease instability (labeled in the inset in Fig. 4) occurs at the corner of the CS craters at certain preloads, which causes divergence in FEM. Thus, the FEM results for CS craters are only presented before the crease occurs, i.e., $\overline{\sigma}_{pre} = 55$ kPa and $\overline{\sigma}_{pre} = 70$ kPa for CS craters of $b/a = 1$ and $2/3$, respectively. Second, it is obvious that craters with smaller initial volume produce higher suction force under small preload, which is consistent with experimental observations by Nanni et al. [47]. For example, within the same type of craters, shallow craters yield higher suction force than deep ones under the same preload. Comparing SCS and CS craters with the same aspect ratio, SCS craters outperform their CS counterpart because SCS craters have smaller initial volume. This conclusion can be further supported by comparing the hemisphere-shaped crater, i.e., the SCS crater with $b/a = 1$, with the CS crater with $b/a = 2/3$. These two craters have the same initial volume and crater radius, thus exhibit comparable suction forces when $\overline{\sigma}_{pre} \leq 55$ kPa. However, such trend can be easily violated under large preload. For instance, hemispherical crater exhibits larger suction force than shallow SCS crater when $\overline{\sigma}_{pre} > 120$ kPa according to Fig. 4. This is consistent with our previous finding that deeper craters generate higher suction force than shallower ones at full closure [48].

4. Effects of crater area fraction and array pattern

4.1. Simulation

In this section, we extend the FEM approach developed for isolated craters to crater arrays in two different patterns — the square-patterned arrays (SPA) and the hexagon-patterned arrays (HPA), as illustrated in Fig. 5a. Our goal is seeking for the optimal design of the cratered surface that maximizes the suction force of a given polymer sheet. To better elucidate how crater area fraction and pattern affect the suction force, in what follows the crater geometry is fixed as a SCS crater with aspect ratio $b/a = 2/3$ and the polymer matrix is assumed to be incompressible neo-Hookean material with shear modulus $\mu = 47.3$ kPa. Different from simulations for isolated craters where axisymmetric models were used, simulations for crater arrays call for three-dimensional models. According to the nature of their periodicity, representative volume elements of SPA and HPA, i.e., unit cells, were simulated with periodic boundary conditions assigned. Bottom-up views of the simulation schemes are graphically expressed in Figs. 5b and 5c, respectively. For SPA, the unit cell is a square containing a crater at the center. The size of the unit square and the radius of the crater are denoted as D_s and a, respectively. Geometric symmetries allow us to only model a quarter of the unit. The x and y planes are symmetric planes as shown by the dash–dot lines. Periodicity in both x and y directions dictates the square unit cell remains as a square under uniaxial compression. In other words, the displacement in the y direction of all nodes on $y = D_s$ plane are constrained to be the same, i.e., $u_y^{all} = u_y^r$ where superscript '*all*' represents all nodes on that plane and 'r' corresponds to the reference node which is highlighted by red. Similarly, $u_x^{all} = u_x^r$. As for HPA, the unit cell is a hexagon which remains as a hexagon under uniaxial compression. Therefore, a 30°–60°–90° triangle suffices for the simulation by enforcing $u_y^{all} = u_y^r$ on $y = D_h$ plane and 60° plane remains 60°, i.e., $u_y^i = \sqrt{3}u_x^i$ where superscript 'i' denotes each individual node itself. It is worth noting that modeling a unit cell rather than the entire specimen is for the sake of reducing model size. But one should be aware that such a simplification can be adopted only when the array consists of a sufficient number of craters such that only a small fraction of craters are near the edge of the array where periodic boundary conditions break down. The simulated loading–unloading process of craters in SPA and HPA can be visualized in the supplementary video.

4.2. Results

4.2.1. Suction force of a unit cell

The FEM results of normalized suction force $F/(p_0A_0)$ produced by a unit cell of SPA and HPA are given in Fig. 6a and Fig. 6b, respectively, where $A_0 = \pi a^2$ is the projected area of the crater at Stage 0. For SPA, the largest possible crater area fraction is $\pi/4 \approx 78.5\%$ thus we consider the following $\phi = 8.73, 19.6, 34.9, 54.5, 64.9$ and 71.2%, corresponding to $a/D_s = 1/3, 1/2, 2/3, 5/6, 10/11$ and $20/21$. For HPA, a higher crater area fraction $\phi = 80\%$ can be achieved hence it was also simulated. For comparison, results for isolated craters, i.e., $\phi \to 0$ are also plotted in Fig. 6a and Fig. 6b as dashed black curves. Analysis of the two plots can be performed in the follows. First, it is evident that in both plots, $\phi = 8.73\%$ overlaps with the black

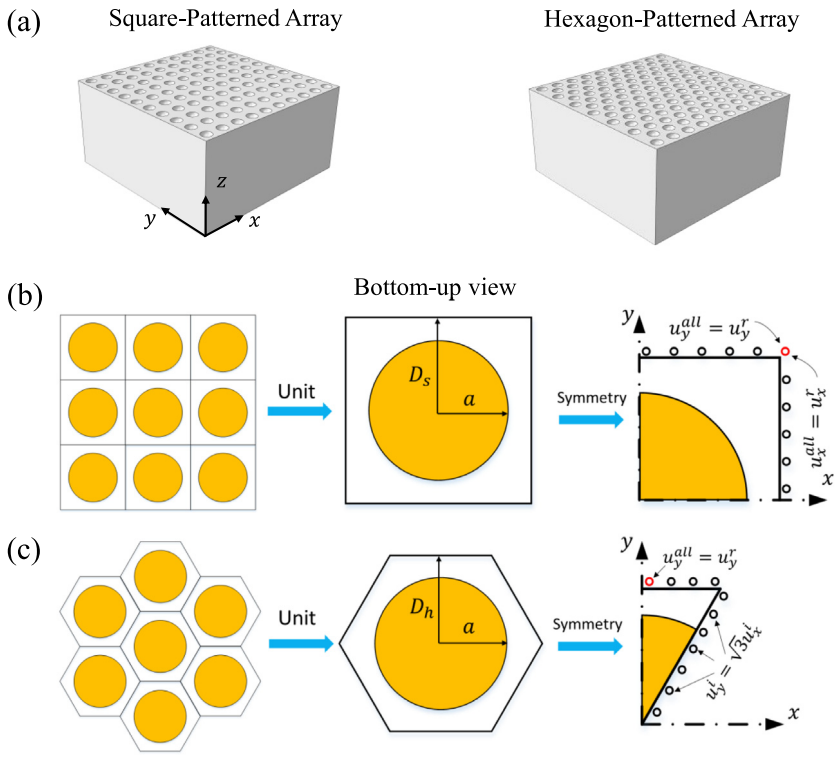

Fig. 5. (a) Two designs for cratered surfaces: square-patterned-arrays (SPA), and hexagon-patterned-arrays (HPA). (b)–(c) Bottom-up views of the arrays, unit cells, FEM cell and boundary conditions used in simulation. Geometric periodicity and symmetry are implemented for reducing model size.

dashed curve, which represents $\phi \to 0$. This is consistent with our previous claim that crater arrays with $\phi < 11.1\%$ should recover the isolated crater scenario. Second, for both SPA and HPA, when $\phi < 54.5\%$, the normalized suction force monotonically increases with the preload till full closure is attained. When $\phi \geq 54.5\%$, a non-monotonic suction–preload relation is found. This is because when the crater area fraction is large, the overall structural stiffness of the unit cell is low, leading to limited recovery and hence small projected area A_2 after unloading, which is evident in the supplementary video. Also, this reduction becomes more conspicuous when the area fraction is large, say $\phi = 71.2\%$ and 80% in Fig. 6b.

To better compare the behaviors of the crater arrays with various area fractions under different preloads, we also plot the suction force of crater unit cell (F) normalized by that of an isolated crater (F_{iso}) as a function of ϕ in Fig. 6c. Solid curves plot results under a small preload $\overline{\sigma}_{pre} = 50$ kPa; while dashed curves represent large preload $\overline{\sigma}_{pre} = 120$ kPa under which all craters are fully closed. Again, it can be seen that when $\phi < 11.1\%$, $F/F_{\text{iso}} = 1$, suggesting that the arrayed craters can be treated as isolated craters. When $\overline{\sigma}_{pre} = 50$ kPa, F/F_{iso} increases with area fraction, meaning that the interaction between craters boosts the suction force; while when $\overline{\sigma}_{pre} = 120$ kPa, F/F_{iso} decreases with area fraction, manifesting that interaction between craters impairs the generation of suction force. The reason lies in the fact that arrays with larger ϕ tend to have lower structural stiffness, giving rise to a smaller crater volume V_1 at the compressed stage under the same preload prior to full closure. Therefore, under small preload, smaller V_1 is achieved, leading to larger $F/(p_0A_0)$. However, if the preload is large enough (e.g., $\overline{\sigma}_{pre} = 120$ kPa) to fully close craters, i.e., $V_1 = 0$ for any ϕ, $F/(p_0A_0)$ is only determined by the projected area A_2 at Stage 2. Then larger ϕ produces smaller A_2 due to the lower structural stiffness, diminishing the suction force (see supplementary video). Moreover, this plot indicates that the difference between SPA and HPA is not significant given the same ϕ.

4.2.2. Total suction force of the polymer sheet

Assume that a polymer sheet has a base plane area of A_t with total number of craters denoted as m. The total suction force of the polymer sheet F_t can be computed by summing the suction force produced by all the craters, i.e., $F_t = mF$, where F is the suction force generated by a unit cell. This calculation neglects craters at the edge of the array so it is only true for an array with large number of craters. Normalizing F_t by p_0A_t produces

$$\frac{F_t}{p_0A_t} = m\frac{A_0}{A_t}\frac{F}{p_0A_0} = \phi\frac{F}{p_0A_0} \tag{6}$$

Eq. (6) clearly shows that the normalized suction force is proportional to ϕ and $F/(p_0A_0)$. Thus if $F/(p_0A_0)$ also increases with ϕ, then higher total suction force will be achieved as ϕ gets larger. This is true when the preload is small as can be seen in Fig. 7a and Fig. 7b in which $F_t/(p_0A_t)$ is plotted versus preload $\overline{\sigma}_{pre}$ for various ϕ. When preload $\overline{\sigma}_{pre} \leq 80$ kPa, larger crater area fraction leads to higher suction force for both SPA and HPA. The reasons are twofold. First, as explained above, large ϕ yields higher $F/(p_0A_0)$ according to Eq. (3) under small preloads. Second, larger ϕ means more craters are contributing to the total suction force based on Eq. (6). For example, by fixing $\overline{\sigma}_{pre} = 50$ kPa, $F_t/(p_0A_t)$ as a function of ϕ is presented by the shaded bars in Fig. 7c, in which $F_t/(p_0A_t)$ monotonically grows with increasing ϕ for both SPA and HPA. However, under large preload, $F/(p_0A_0)$ may decrease with crater area fraction (see Fig. 6c). Therefore, the total suction force may exhibit a non-monotonic dependence on ϕ. Hence there exists a maximum total suction force at intermediate ϕ. For instance, if fixing $\overline{\sigma}_{pre} = 120$ kPa, the largest $F_t/(p_0A_t)$ is achieved when $54.5\% \leq \phi \leq 64.9\%$ as shown by the solid bars in Fig. 7c.

The suction force of crater arrays inherently depends the on preload, and the largest total suction force that can be achieved is $0.34p_0A_t$ by HPA with $\phi = 80\%$ under the preload $\overline{\sigma}_{pre} = 80$ kPa given by the orange curve in Fig. 7b. But one has to be aware that results presented in Fig. 7 are exclusively applicable to SCS

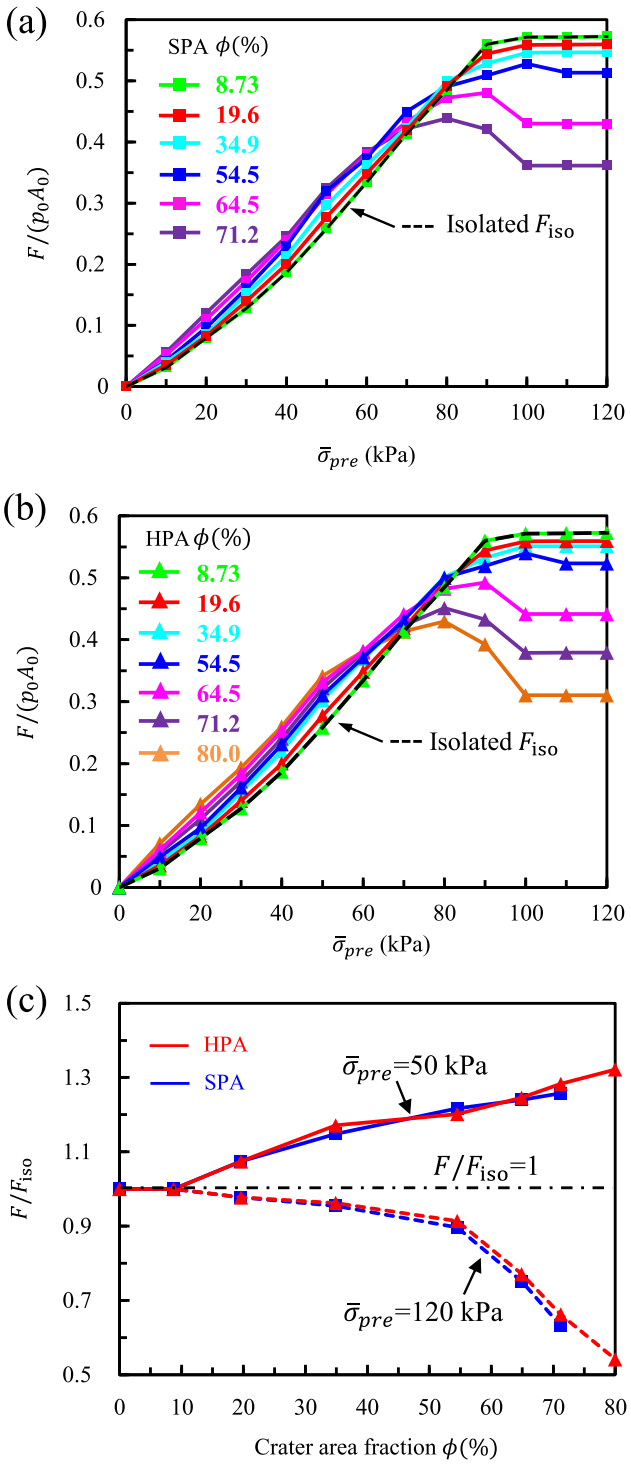

Fig. 6. (a)–(b) Normalized suction force of a unit cell $F/(p_0A_0)$ as a function of $\bar{\sigma}_{pre}$ for (a) SPA and (b) HPA. (c) Suction force of a unit cell normalized by that of an isolated crater, i.e., F/F_{iso}, as a function of area fraction under two different preloads – a small preload $\bar{\sigma}_{pre}$ = 50 kPa, and a large preload $\bar{\sigma}_{pre}$ = 12 kPa under which crater is fully closed at Stage 1.

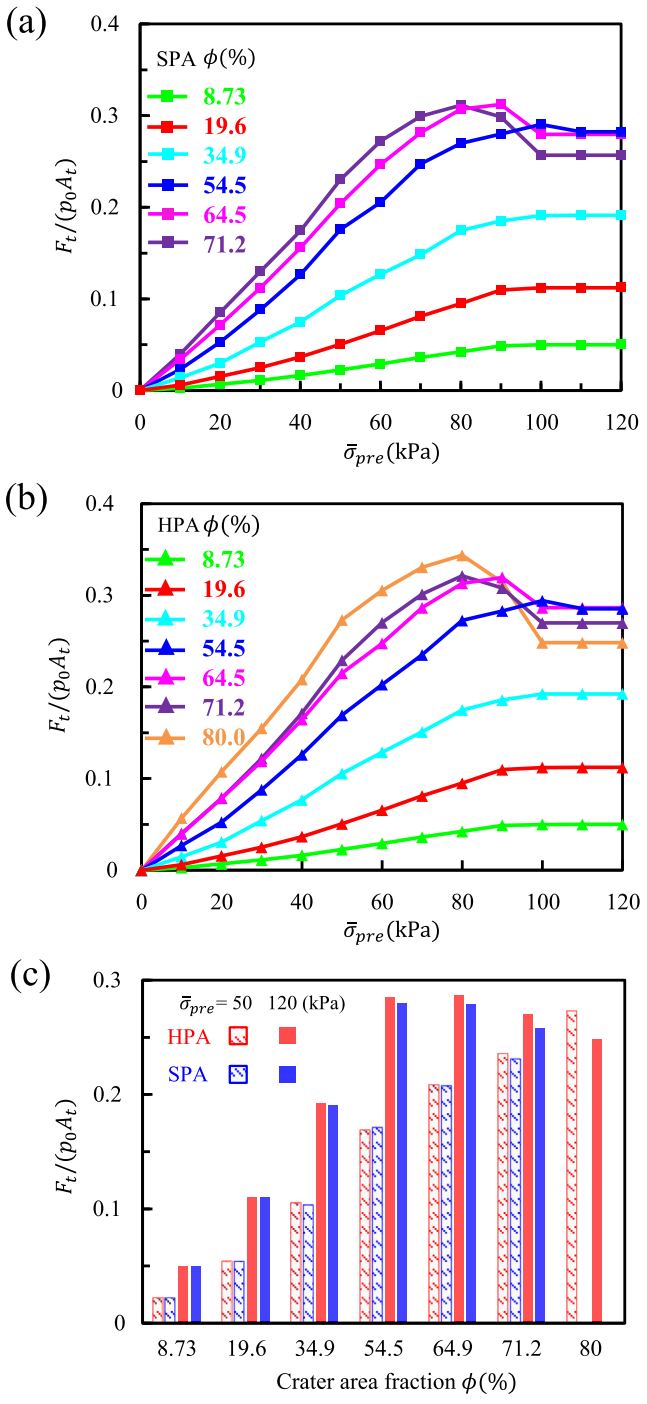

Fig. 7. (a)–(b) Normalized total suction force of the polymer sheet $F_t/(p_0A_t)$ as a function of $\bar{\sigma}_{pre}$ for (a) SPA and (b) HPA. (c) Normalized total suction force of the polymer sheet $F_t/(p_0A_t)$ for various area fractions under two different preloads – a small preload $\bar{\sigma}_{pre}$ = 50 kPa, and a large preload $\bar{\sigma}_{pre}$ = 120 kPa under which craters are fully closed at Stage 1.

crater with aspect ratio $b/a = 2/3$ and neo-Hookean material property $\mu = 47.3$ kPa. For more information regarding how material stiffness and crater shape would affect the suction force of an isolated crater, please refer to our previous publication [48].

5. Conclusions

Suction forces generated by cratered surfaces depend on crater shape, crater area fraction, array pattern, and applied preload. We adopted experimentally validated FEM approach to reveal the effect of each factor. It was found out that for a given aspect ratio and preload, isolated spherical-cap-shaped (SCS) craters always produce higher suction forces than isolated cylinder-shaped (CS) craters. Fixing SCS craters with aspect ratio of 2/3, we investigated

two cratered arrays, square-patterned array (SPA) and hexagon-patterned array (HPA), with various crater area fractions under different preload. It was discovered that the suction force of both the unit cell and the overall array has non-monotonic dependency on the crater area fraction under large preload. In fact, full closure of the crater may impair the suction effect. To achieve the highest suction force, a moderately large preload and area fraction is desired. The suction performance of SPA is quite comparable to HPA except that HPA enables larger area fraction. This study provides very useful insights for the design of cratered surfaces which constitute future dry adhesives for robots and medical adhesives.

Acknowledgments

Authors acknowledge the support from the National Science Foundation (NSF), United States Division of Civil, Mechanical and Manufacturing Innovation (CMMI) award (Grant No. 1663551). Liu Wang and Shutao Qiao acknowledge the Warren A. and Alice L. Meyer endowed graduate fellowship awarded by the Cockrell School of Engineering at the University of Texas at Austin. Kyoung-Ho Ha acknowledge the Philip C. and Linda L. Lewis Foundation Graduate Fellowship in Mechanical Engineering at the University of Texas at Austin.

Declaration of competing interest

The authors declare that there is no conflict of interest.

Appendix A. Supplementary data

Supplementary material related to this article can be found online at https://doi.org/10.1016/j.eml.2019.100496.

References

[1] I. Webster, Recent developments in pressure-sensitive adhesives for medical applications, Int. J. Adhes. Adhes. 17 (1) (1997) 69–73.
[2] M. Donkerwolcke, F. Burny, D. Muster, Tissues and bone adhesives—historical aspects, Biomaterials 19 (16) (1998) 1461–1466.
[3] C. Creton, Pressure-sensitive adhesives: an introductory course, MRS Bull. 28 (6) (2003) 434–439.
[4] Z. Czech, A. Kowalczyk, Pressure-sensitive adhesives for medical applications, in: Wide Spectra of Quality Control, InTech, 2011.
[5] K. Kawahara, K. Tojo, Skin irritation in transdermal drug delivery systems: a strategy for its reduction, Pharm. Res. 24 (2) (2007) 399.
[6] W.A. Christoffers, P.J. Coenraads, M.L. Schuttelaar, Bullous allergic reaction caused by colophonium in medical adhesives, Contact Dermatitis 70 (4) (2014) 256–257.
[7] I. Hwang, H.N. Kim, M. Seong, S.H. Lee, M. Kang, H. Yi, W.G. Bae, M.K. Kwak, H.E. Jeong, Multifunctional smart skin adhesive patches for advanced health care, Adv. Healthc. Mater. (2018) 1800275.
[8] A. Del Campo, E. Arzt, Design parameters and current fabrication approaches for developing bioinspired dry adhesives, Macromol. Biosci. 7 (2) (2007) 118–127.
[9] M.K. Kwak, H.E. Jeong, T.I. Kim, H. Yoon, K.Y. Suh, Bio-inspired slanted polymer nanohairs for anisotropic wetting and directional dry adhesion, Soft Matter 6 (9) (2010) 1849–1857.
[10] A. Pattantyus-Abraham, J. Krahn, C. Menon, Recent advances in nanostructured biomimetic dry adhesives, Front. Bioeng. Biotechnol. 1 (22) (2013).
[11] R. Sahay, H.Y. Low, A. Baji, F. Shaohui, K.L. Wood, A state-of-the-art review and analysis on the design of dry adhesion materials for applications such as climbing micro-robots, RSC Adv. (2015).
[12] L. Xiaosong, T. Dashuai, L. Hongyu, B. Pengpeng, L. Zheyu, M. Liran, M. Yonggang, T. Yu, Recent developments in gecko-inspired dry adhesive surfaces from fabrication to application, Surf. Topogr. Metrol. Prop. (2019).
[13] S. Erramilli, J. Genzer, Influence of surface topography attributes on settlement and adhesion of natural and synthetic species, Soft Matter (2019).
[14] K. Autumn, Y.A. Liang, S.T. Hsieh, W. Zesch, W.P. Chan, T.W. Kenny, R. Fearing, R.J. Full, Adhesive force of a single gecko foot-hair, Nature 405 (6787) (2000) 681–685.
[15] H. Gao, H. Yao, Shape insensitive optimal adhesion of nanoscale fibrillar structures, Proc. Natl. Acad. Sci. USA 101 (21) (2004) 7851–7856.
[16] K. Autumn, A. Dittmore, D. Santos, M. Spenko, M. Cutkosky, Frictional adhesion: a new angle on gecko attachment, J. Exp. Biol. 209 (18) (2006) 3569–3579.
[17] Y. Cho, H.K. Minsky, Y. Jiang, K. Yin, K.T. Turner, S. Yang, Shear adhesion of tapered nanopillar arrays, ACS Appl. Mater. Interfaces 10 (13) (2018) 11391–11397.
[18] Y. Cho, G. Kim, Y. Cho, S.Y. Lee, H. Minsky, K.T. Turner, D.S. Gianola, S. Yang, Orthogonal control of stability and tunable dry adhesion by tailoring the shape of tapered nanopillar arrays, Adv. Mater. 27 (47) (2015) 7788–7793.
[19] M.K. Kwak, C. Pang, H.E. Jeong, H.N. Kim, H. Yoon, H.S. Jung, K.Y. Suh, Towards the next level of bioinspired dry adhesives: new designs and applications, Adv. Funct. Mater. 21 (19) (2011) 3606–3616.
[20] M. Kamperman, E. Kroner, A. del Campo, R.M. McMeeking, E. Arzt, Functional adhesive surfaces with gecko effect: the concept of contact splitting, Adv. Energy Mater. 12 (5) (2010) 335–348.
[21] E.P. Chan, C. Greiner, E. Arzt, A.J. Crosby, Designing model systems for enhanced adhesion, MRS Bull. 32 (06) (2007) 496–503.
[22] H. Yao, H. Gao, Mechanics of robust and releasable adhesion in biology: bottom-up designed hierarchical structures of gecko, J. Mech. Phys. Solids 54 (6) (2006) 1120–1146.
[23] R. Hensel, K. Moh, E. Arzt, Engineering micropatterned dry adhesives: from contact theory to handling applications, Adv. Funct. Mater. (2018) 1800865.
[24] C. Greiner, E. Arzt, A. del Campo, Hierarchical gecko-like adhesives, Adv. Mater. 21 (4) (2009) 479–482.
[25] W.G. Bae, D. Kim, M.K. Kwak, L. Ha, S.M. Kang, K.Y. Suh, Enhanced skin adhesive patch with modulus-tunable composite micropillars, Adv. Healthc. Mater. 2 (1) (2013) 109–113.
[26] M.P. Murphy, B. Aksak, M. Sitti, Gecko-inspired directional and controllable adhesion, Small 5 (2) (2009) 170–175.
[27] Y. Mengüç, S.Y. Yang, S. Kim, J.A. Rogers, M. Sitti, Gecko-inspired controllable adhesive structures applied to micromanipulation, Adv. Funct. Mater. 22 (6) (2012) 1246–1254.
[28] S. Chary, J. Tamelier, K. Turner, A microfabricated gecko-inspired controllable and reusable dry adhesive, Smart Mater. Struct. 22 (2) (2013) 025013.
[29] C. Greiner, A.D. Campo, E. Arzt, Adhesion of bioinspired micropatterned surfaces: effects of pillar radius, aspect ratio, and preload, Langmuir 23 (7) (2007) 3495–3502.
[30] T. Kim, J. Park, J. Sohn, D. Cho, S. Jeon, Bioinspired, highly stretchable, and conductive dry adhesives based on 1d-2d hybrid carbon nanocomposites for all-in-one ecg electrodes, Acs Nano 10 (4) (2016) 4770–4778.
[31] D.S. Kim, H.S. Lee, J. Lee, S. Kim, K.-H. Lee, W. Moon, T.H.J.M.T. Kwon, Replication of high-aspect-ratio nanopillar array for biomimetic gecko foot-hair prototype by UV nano embossing with anodic aluminum oxide mold, 13(5-6) (2007) 601–606.
[32] S. Buhl, C. Greiner, A.d. Campo, E. Arzt, Humidity influence on the adhesion of biomimetic fibrillar surfaces, Int. J. Mater. Res. 100 (8) (2009) 1119–1126.
[33] N. Cadirov, J.A. Booth, K.L. Turner, J.N. Israelachvili, Influence of humidity on grip and release adhesion mechanisms for gecko-inspired microfibrillar surfaces, ACS Appl. Mater. Interfaces 9 (16) (2017) 14497–14505.
[34] N.S. Pesika, H. Zeng, K. Kristiansen, B. Zhao, Y. Tian, K. Autumn, J. Israelachvili, Gecko adhesion pad: a smart surface?, J. Phys.: Condens. Matter 21 (46) (2009) 464132.
[35] S. Akerboom, J. Appel, D. Labonte, W. Federle, J. Sprakel, M. Kamperman, Enhanced adhesion of bioinspired nanopatterned elastomers via colloidal surface assembly, J. Royal Soc. Interface 12 (102) (2015) 20141061.
[36] M.K. Choi, O.K. Park, C. Choi, S. Qiao, R. Ghaffari, J. Kim, D.J. Lee, M. Kim, W. Hyun, S.J. Kim, H.J. Hwang, S.H. Kwon, T. Hyeon, N. Lu, D.H. Kim, Cephalopod-inspired miniaturized suction cups for smart medical skin, Adv. Healthc. Mater 5 (1) (2016) 80–87.
[37] W.-Y. Chang, Y. Wu, Y.-C. Chung, Facile fabrication of ordered nanostructures from protruding nanoballs to recessional nanosuckers via solvent treatment on covered nanosphere assembled monolayers, Nano Lett. 14 (3) (2014) 1546–1550.
[38] F. Tramacere, L. Beccai, M. Kuba, A. Gozzi, A. Bifone, B. Mazzolai, The morphology and adhesion mechanism of Octopus vulgaris suckers, 2013.
[39] S. Baik, D.W. Kim, Y. Park, T.-J. Lee, S. Ho Bhang, C. Pang, A wet-tolerant adhesive patch inspired by protuberances in suction cups of octopi, Nature 546 (7658) (2017) 396–400.
[40] S. Baik, J. Kim, H.J. Lee, T.H. Lee, C. Pang, Highly adaptable and biocompatible octopus-like adhesive patches with meniscus-controlled unfoldable 3d microtips for underwater surface and hairy skin, Adv. Sci. (2018) 1800100.
[41] V. Tinnemann, L. Hernández, S.C. Fischer, E. Arzt, R. Bennewitz, R. Hensel, In situ observation reveals local detachment mechanisms and suction effects in micropatterned adhesives, Adv. Funct. Mater. (2019) 1807713.

[42] B. Aksak, M.P. Murphy, M. Sitti, Gecko inspired micro-fibrillar adhesives for wall climbing robots on micro/nanoscale rough surfaces, in: Proc. Robotics and Automation, 2008. ICRA 2008. IEEE International Conference on, IEEE, pp. 3058–3063.
[43] H. Lee, D.S. Um, Y. Lee, S. Lim, Kim, H. Ko, Octopus-inspired smart adhesive pads for transfer printing of semiconducting nanomembranes, Adv. Mater. 28 (34) (2016) 7457–7465.
[44] S. Baik, H.J. Lee, D.W. Kim, J.W. Kim, Y. Lee, C. Pang, Bioinspired adhesive architectures: from skin patch to integrated bioelectronics, Adv. Mater. (2019) e1803309.
[45] https://megatinycorp.com/, M. A.-G. C.
[46] Y.C. Chen, H. Yang, Octopus-inspired assembly of nanosucker arrays for dry/wet adhesion, ACS Nano 11 (6) (2017) 5332–5338.
[47] G. Nanni, D. Fragouli, L. Ceseracciu, A. Athanassiou, Adhesion of elastomeric surfaces structured with micro-dimples, Appl. Surf. Sci. 326 (2015) 145–150.
[48] S. Qiao, L. Wang, H. Jeong, G.J. Rodin, N. Lu, Suction effects in cratered surfaces, J. R. Soc. Interface 14 (135) (2017) 20170377.
[49] Shutao Qiao L.W., Kyoung-Ho Ha, Nanshu Lu, Suction effects of craters underwater, Soft Matter (2018).
[50] L. Wang, S. Qiao, N. Lu, Effects of surface tension on the suction forces generated by miniature craters, Extreme Mech. Lett. 15 (2017) 130–138.
[51] D.L. Henann, K. Bertoldi, Modeling of elasto-capillary phenomena, Soft Matter 10 (5) (2014) 709–717.
[52] B. Roman, J. Bico, Elasto-capillarity: deforming an elastic structure with a liquid droplet, J. Phys.: Condens. Matter 22 (2010) 493110.
[53] L. Afferrante, G. Carbone, G. Demelio, N. Pugno, Adhesion of elastic thin films: double peeling of tapes versus axisymmetric peeling of membranes, Tribol. Lett. 52 (3) (2013) 439–447.
[54] D. Ge, T. Matsuno, Y. Sun, C. Ren, Y. Tang, S. Ma, Quantitative study on the attachment and detachment of a passive suction cup, Vacuum 116 (2015) 13–20.
[55] J. Liu, K. Tanaka, L. Bao, I. Yamaura, Analytical modelling of suction cups used for window-cleaning robots, Vacuum 80 (6) (2006) 593–598.